



# Microflare Heating of a Solar Active Region Observed with *NuSTAR*, *Hinode/XRT*, and *SDO/AIA*

Paul J. Wright<sup>1</sup>, Iain G. Hannah<sup>1</sup>, Brian W. Grefenstette<sup>2</sup>, Lindsay Glesener<sup>3</sup>, Säm Krucker<sup>4,5</sup>, Hugh S. Hudson<sup>1,4</sup>, David M. Smith<sup>6</sup>, Andrew J. Marsh<sup>6</sup>, Stephen M. White<sup>7</sup>, and Matej Kuhar<sup>5</sup>

<sup>1</sup> SUPA School of Physics & Astronomy, University of Glasgow, Glasgow G12 8QQ, UK; [paul.wright@glasgow.ac.uk](mailto:paul.wright@glasgow.ac.uk)

<sup>2</sup> Cahill Center for Astrophysics, 1216 E. California Blvd., California Institute of Technology, Pasadena, CA 91125, USA

<sup>3</sup> School of Physics & Astronomy, University of Minnesota—Twin Cities, Minneapolis, MN 55455, USA

<sup>4</sup> Space Sciences Laboratory University of California, Berkeley, CA 94720, USA

<sup>5</sup> University of Applied Sciences and Arts Northwestern Switzerland, 5210 Windisch, Switzerland

<sup>6</sup> Santa Cruz Institute of Particle Physics and Department of Physics, University of California, Santa Cruz, CA 95064, USA

<sup>7</sup> Air Force Research Laboratory, Space Vehicles Directorate, 3550 Aberdeen Ave. SE, Kirtland AFB, NM 87117, USA

Received 2017 April 12; revised 2017 June 16; accepted 2017 June 16; published 2017 July 31

## Abstract

*NuSTAR* is a highly sensitive focusing hard X-ray (HXR) telescope and has observed several small microflares in its initial solar pointings. In this paper, we present the first joint observation of a microflare with *NuSTAR* and *Hinode/XRT* on 2015 April 29 at  $\sim 11:29$  UT. This microflare shows the heating of material to several million Kelvin, observed in soft X-rays with *Hinode/XRT*, and was faintly visible in the extreme ultraviolet with *SDO/AIA*. For three of the four *NuSTAR* observations of this region (pre-flare, decay, and post-flare phases), the spectrum is well fitted by a single thermal model of 3.2–3.5 MK, but the spectrum during the impulsive phase shows additional emission up to 10 MK, emission equivalent to the A0.1 *GOES* class. We recover the differential emission measure (DEM) using *SDO/AIA*, *Hinode/XRT*, and *NuSTAR*, giving unprecedented coverage in temperature. We find that the pre-flare DEM peaks at  $\sim 3$  MK and falls off sharply by 5 MK; but during the microflare’s impulsive phase, the emission above 3 MK is brighter and extends to 10 MK, giving a heating rate of about  $2.5 \times 10^{25} \text{ erg s}^{-1}$ . As the *NuSTAR* spectrum is purely thermal, we determined upper limits on the possible non-thermal bremsstrahlung emission. We find that for the accelerated electrons to be the source of heating, a power-law spectrum of  $\delta \geq 7$  with a low-energy cutoff  $E_c \lesssim 7 \text{ keV}$  is required. In summary, this first *NuSTAR* microflare strongly resembles much more powerful flares.

**Key words:** Sun: activity – Sun: corona – Sun: X-rays, gamma rays

## 1. Introduction

Solar flares are rapid releases of energy in the corona and are typically characterized by impulsive emission in Hard X-rays (HXR) followed by brightening in Soft X-rays (SXR) and Extreme Ultraviolet (EUV) indicating that electrons have been accelerated as well as material heated.

Flares are observed to occur over many orders of magnitude, from large X-Class *GOES* (*Geostationary Operational Environmental Satellite*) flares down to A-class microflares. Observations from *RHESSI* (*Reuven Ramaty High Energy Solar Spectroscopic Imager*; Lin et al. 2002) have shown that microflares occur exclusively in active regions (ARs), like larger flares, as well as heating material  $> 10 \text{ MK}$  and accelerating electrons to  $> 10 \text{ keV}$  (Christe et al. 2008; Hannah et al. 2008, 2011). Although energetically these events are about six orders of magnitude smaller than large flares, it shows that the same physical processes are at work to impulsively release energy. There should be smaller events beyond *RHESSI*’s sensitivity but so far there have either only been limited SXR observations from *SphinX* (Gburek et al. 2011) or indirect evidence of non-thermal emission from *IRIS* observations (e.g., Testa et al. 2014). There are also energetically smaller events observed in thermal EUV/SXR emission that occur outside ARs (Krucker et al. 1997; Aschwanden et al. 2000; Parnell & Jupp 2000).

Smaller flares occur considerably more often than large flares with their frequency distribution behaving as a negative power law (e.g., Hannah et al. 2011). It is not clear how small flare-like events can be, with Parker (1988) suggesting that small-scale reconnection events (“nanoflares”) are on the order of  $\sim 10^{24} \text{ erg}$ . However, at this scale, flares are likely too small to be individually observed, and only the properties of the unresolved ensemble could be determined (Glencross 1975). Nor is it clear whether the flare frequency distribution is steep enough (requiring  $\alpha > 2$ , Hudson 1991) so that there are enough small events to keep the solar atmosphere consistently heated. It is therefore crucial to probe how small flares can be while still remaining distinct, and how their properties relate to flares and microflares.

With the launch of the *Nuclear Spectroscopic Telescope Array* (*NuSTAR*; Harrison et al. 2013), HXR (2.5–78 keV) observations of faint, previously undetectable solar sources can be obtained. In comparison to *RHESSI*, *NuSTAR* has over a  $10\times$  larger effective area and a much smaller background counting rate. However, *NuSTAR* was designed for astrophysical observations and is therefore not optimized for observations of the Sun. This leads to various technical challenges (see Grefenstette et al. 2016), but *NuSTAR* is nevertheless a unique instrument for solar observations and has pointed at the Sun several times. *NuSTAR* has observed several faint sources from quiescent ARs (Hannah et al. 2016) and emission from an occulted flare, in the EUV late phase (Kuhar et al. 2017). *NuSTAR* has also observed several small microflares during its solar observations, one showing the time evolution and spectral emission (Glesener et al. 2017).



Original content from this work may be used under the terms of the [Creative Commons Attribution 3.0 licence](https://creativecommons.org/licenses/by/3.0/). Any further distribution of this work must maintain attribution to the author(s) and the title of the work, journal citation and DOI.

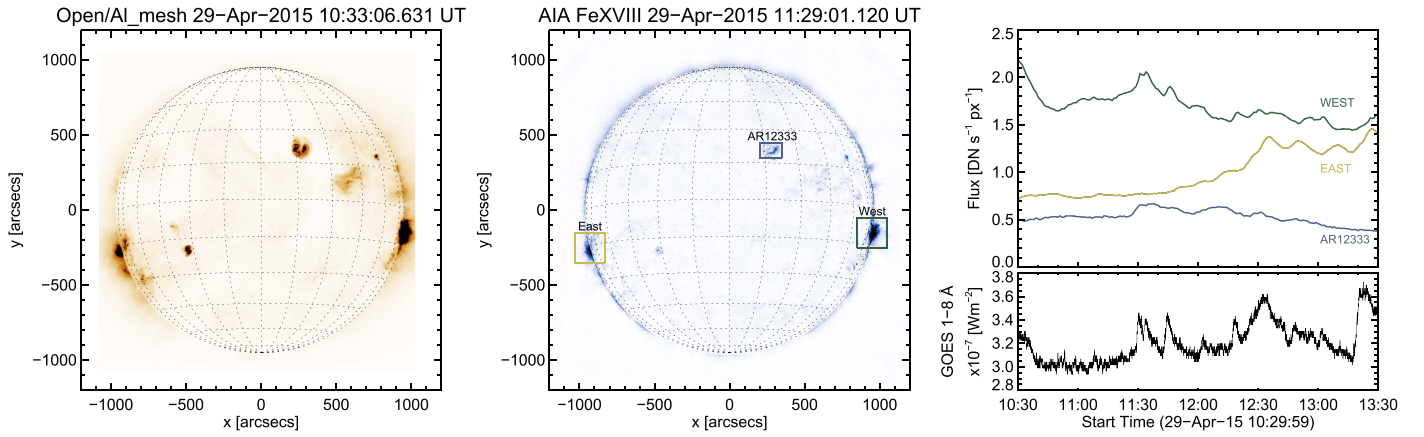


**Figure 1.** Overview of the *SDO*/AIA 94 Å Fe XVIII conditions during the times of the *NuSTAR* and *Hinode*/XRT observations prior to the AR 12333 microflare onset. (Left) Full-disk image from *Hinode*/XRT one hour prior to the microflare onset. (Middle) Full-disk *SDO*/AIA 94 Å Fe XVIII image at the peak of the microflare impulsive phase with the ARs indicated. The *SDO*/AIA 94 Å Fe XVIII light curves from these three regions are shown in comparison to the full-disk *GOES* 1–8 Å SXR flux (right). All of the regions are producing several microflares during these times, but those from AR 12333 are hidden in the *GOES* light curve as those from the two limb regions are brighter.

In this paper, we present *NuSTAR* imaging spectroscopy of the first microflare jointly observed with *Hinode*/XRT (Golub et al. 2007; Kosugi et al. 2007) and *SDO*/AIA (Pesnell et al. 2012; Lemen et al. 2012). This microflare occurred on 2015 April 29 within AR 12333, and showed distinctive loop heating visible with *NuSTAR*, *Hinode*/XRT, and the hottest EUV channels of *SDO*/AIA up to 10 MK. We first present an overview of the *SDO*/AIA and *Hinode*/XRT observations in Section 2, followed by *NuSTAR* data analysis in Section 3. In Section 4, we concentrate on the impulsive phase of the microflare and perform differential emission measure (DEM) analysis. Finally, in Section 5, we look at the microflare energetics in terms of thermal and non-thermal emission.

## 2. SDO/AIA and Hinode/XRT Event Overview

The microflare from AR 12333 occurred during a time when there were two brighter ARs on the disk, as can be seen in Figure 1. Both of these ARs, on either limb, were producing microflares that dominate the overall *GOES* 1–8 Å SXR light curve (Figure 1, right panels). *GOES* is spatially integrated, but the contributions from each region can be determined by using the hotter Fe XVIII component of the *SDO*/AIA 94 Å images. The Fe XVIII line contribution to the *SDO*/AIA 94 Å channel peaks at  $\log_{10} T = 6.85$  K ( $\sim 7$  MK) and can be recovered using a combination of the *SDO*/AIA channels (Reale et al. 2011; Testa & Reale 2012; Warren et al. 2012; Del Zanna 2013). Here we use the approach of Del Zanna (2013),

$$F(\text{Fe XVIII}) \approx F(94 \text{ Å}) - \frac{F(211 \text{ Å})}{120} - \frac{F(171 \text{ Å})}{450}, \quad (1)$$

where  $F(\text{Fe XVIII})$  is the Fe XVIII flux [ $\text{DN s}^{-1} \text{px}^{-1}$ ] and  $F(94 \text{ Å})$ ,  $F(171 \text{ Å})$ , and  $F(211 \text{ Å})$  are the equivalent fluxes in the *SDO*/AIA 94, 171, and 211 Å channels.

*Hinode*/XRT observed AR 12333 in a high-cadence mode ( $\sim 2$ – $3$  minutes), cycling through five different filter channels centered on this region. Full-disk synoptic images were obtained before and after this observation mode (Figure 1). Figure 2 shows the main loops of the region rapidly brightening, indicating that energy is being released to heat

these loops. This is apparent in the SXR channels from *Hinode*/XRT and *SDO*/AIA 94 Å Fe XVIII, but not in the cooler EUV channels from *SDO*/AIA, so we conclude that the heating is mostly above 3 MK. For the  $95'' \times 45''$  loop region shown in Figure 2, we produce the time profile of the microflares in each of these SXR and EUV channels, shown in Figure 3. These light curves have been obtained after processing via the instrument preparation routines, de-rotation of the solar disk (to  $\sim 11:29$  UT), and manual alignment of *Hinode*/XRT Be-Thin to the  $1''$  downsampled *SDO*/AIA 94 Å Fe XVIII data. Here we again see that the microflare activity is only occurring in the channels sensitive to the hottest material, i.e., the SXR ones from *Hinode*/XRT and *SDO*/AIA 94 Å Fe XVIII. This activity is in the form of three distinctive peaks, with the first, and largest, impulsively starting at  $\sim 11:29$  UT. This is clear in the SXR (with the exception of the low signal-to-noise *Hinode*/XRT Be-Thick channel) and *SDO*/AIA 94 Å Fe XVIII light curves, all showing similar time profiles.

## 3. NuSTAR Data Analysis

*NuSTAR* is an imaging spectrometer with high sensitivity to X-rays over 2.5–78 keV (Harrison et al. 2013). *NuSTAR* consists of two identical telescopes, each with the same  $12' \times 12'$  field of view (Madsen et al. 2015) and is composed of Wolter-I type optics that directly focus X-rays onto the focal-plane modules (FPMA and FPMB) 10 m behind. These focal-plane modules each contain CdZnTe detectors with  $64 \times 64$  pixels providing the time, energy, and location of the incoming X-rays. The readout time per event is 2.5 ms, and *NuSTAR* accepts a maximum throughput of 400 counts  $\text{s}^{-1}$  for each focal-plane module. This makes *NuSTAR* highly capable of observing weak thermal or non-thermal X-ray sources from the Sun (Grefenstette et al. 2016). However, as it is optimized for astrophysics targets, solar pointings have limitations. In particular, the low detector readout and large effective area produce high detector deadtime even for modest levels of solar activity, restricting the spectral dynamic range, and only detecting X-rays at the lowest energies (Grefenstette et al. 2016; Hannah et al. 2016). *NuSTAR* solar observations are therefore from times of weak solar activity, ideally when the *GOES* 1–8 Å flux is below B-level. An overview of the initial

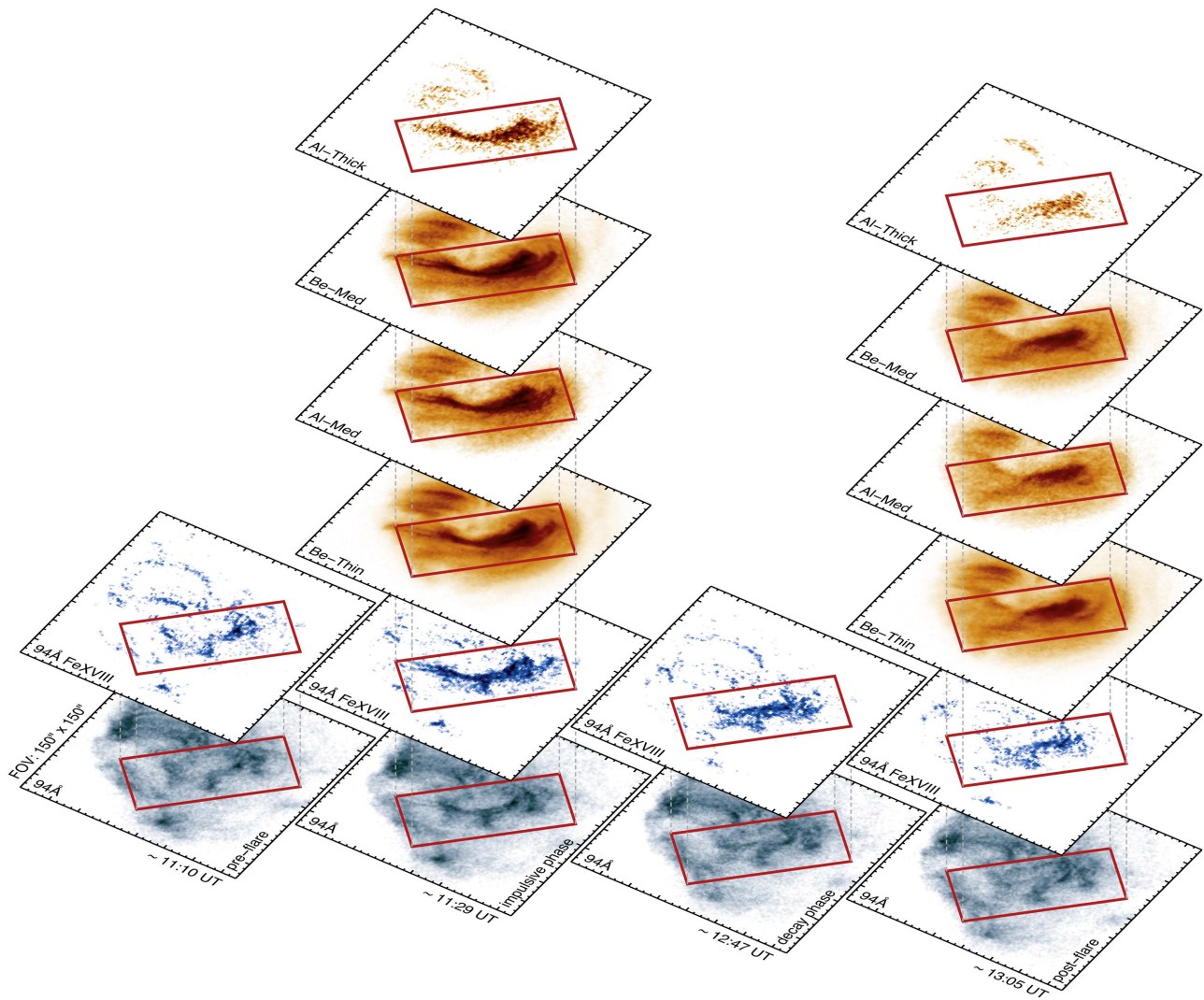


**Figure 2.** Comparison of AR 12333 from *SDO*/AIA and *Hinode*/XRT at the times of *NuSTAR* observations (pre-flare,  $\sim 11:10$  UT; impulsive phase,  $\sim 11:29$  UT; decay phase,  $\sim 12:47$  UT; and post-flare,  $\sim 13:05$  UT). The loop region ( $95'' \times 45''$ ) used for the light curves and DEM analysis is overplotted as a red rectangle. The loop region is faintly observable in *SDO*/AIA 94 Å with the structure well recovered in the *SDO*/AIA 94 Å Fe XVIII and SXR channels.

*NuSTAR* solar pointings, which began in late 2014, and details of these restrictions are available in Grefenstette et al. (2016). An up-to-date quicklook summary is also available online.<sup>8</sup>

The observations reported here are based around the fourth *NuSTAR* solar pointing, consisting of two orbits of observations covering 2015 April 29 10:50 to 11:50 and 12:27 to 13:27 (Grefenstette et al. 2016). *NuSTAR* completed a full-disk mosaic observation in each orbit consisting of 17 different pointings: the field of view requires 16 different pointings to cover the whole Sun, with some overlaps between each mosaic tile, followed by an additional disk-center pointing (see Figure 4 Grefenstette et al. 2016). This resulted in *NuSTAR* observing AR 12333 four times, each lasting for a few minutes. These times are shown in Figure 3. These data were processed using *NuSTAR* Data Analysis software v1.6.0 and *NuSTAR* CALDB 20160502<sup>9</sup>, which produces an event list for each pointing. We use only single-pixel (“Grade 0”) events (Grefenstette et al. 2016) to minimize the effects of pile-up. Figure 4 shows the resulting *NuSTAR* 2.5–4.5 keV image for each of the four

pointings, and these images are a combination of both FPMA and FPMB with  $\sim 7''$  Gaussian smoothing as the pixel size is less than the full width at half maximum (FWHM) of the optics.

Two of these pointings, the first and last, caught the whole AR, but the other two only caught the lower part as they were observed at the edge of the detector; however, this is the location of the heated loops during the microflares in Figure 2. During some of the observations there was a change in the combination of Camera Head Units (CHUs)—star trackers used to provide pointing information. In those such instances, we used the time range that gave the longest continuous CHU combination instead of the whole duration. Each required a different shift to match the *SDO*/AIA 94 Å Fe XVIII map at that time, and all were within the expected  $1'$  offset (Grefenstette et al. 2016). The alignment was straightforward for the *NuSTAR* maps which caught the whole region but was trickier for those with a partial observation. In those cases (the second and third pointings), emission from another region (slightly to the southwest of AR 12333) were used for the alignment. The resulting overlaps of the aligned *Hinode*/XRT and *NuSTAR* images with *SDO*/AIA 94 Å Fe XVIII are shown in Figure 5. The *NuSTAR* maps in Figure 4 reveal a similar pattern to the

<sup>8</sup> [http://ianan.github.io/nsigh\\_all/](http://ianan.github.io/nsigh_all/)

<sup>9</sup> <https://heasarc.gsfc.nasa.gov/docs/NuSTAR/analysis/>



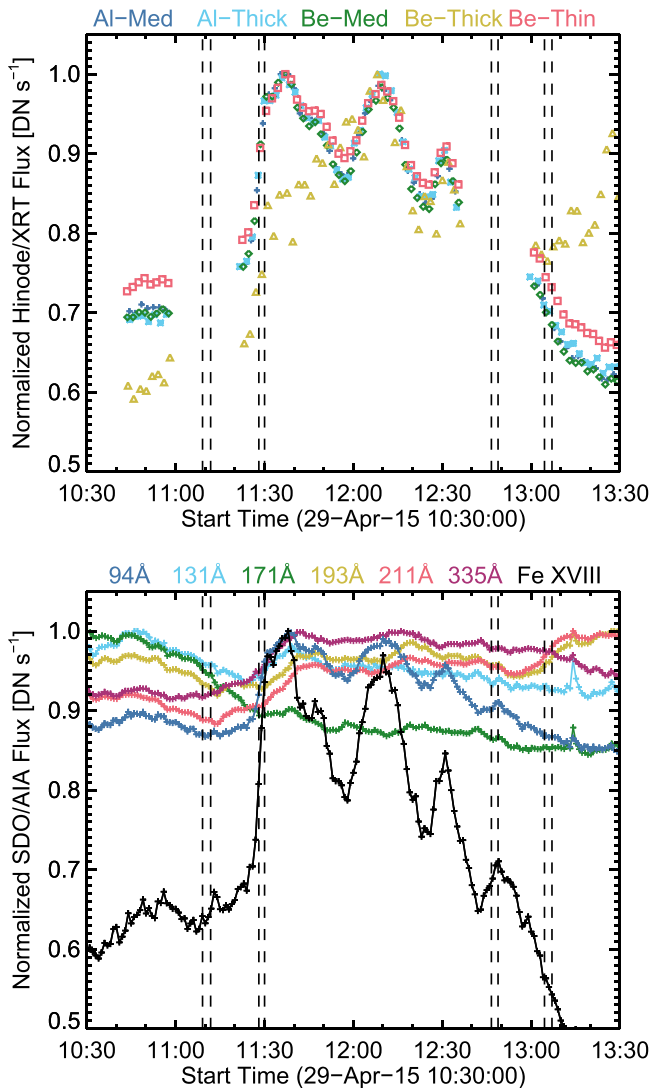


**Figure 3.** Time profiles of the different *Hinode*/XRT (top) and *SDO*/AIA (bottom) channels from the loop region of AR 12333 shown in Figure 2. The vertical bars indicate the four time periods of the *NuSTAR* observation of the same region. The gaps in the *Hinode*/XRT light curves are due to incomplete coverage.

heating seen in EUV and SXR with *SDO*/AIA and *Hinode*/XRT: emission from the whole region before the microflare, with loops in the bottom right brightening as material is heated during the microflare, before fading as the material cools.

### 3.1. *NuSTAR* Spectral Fitting

For each of the *NuSTAR* pointings, we chose a region at the same location, and of the same area, as those used in the *SDO*/AIA and *Hinode*/XRT analysis to produce spectra of the microflare heating. These are circular as the *NuSTAR* software can only calculate the response files for such regions, but do cover the flaring loop region (rectangular box, Figure 2), and are shown in Figure 4. The spectra and *NuSTAR* response files were obtained using *NuSTAR* Data Analysis software v1.6.0. These were then fitted using the XSPEC (Arnaud 1996) software<sup>10</sup>, which simultaneously fits the spectra from each

telescope module (FPMA and FPMB) instead of just adding the data sets. We also use XSPEC as it allows us to find the best-fit solution using Cash statistics (Cash 1979), which helps with the non-Gaussian uncertainties we have for the few counts at higher temperatures.

We fitted the spectra with a single thermal model, using the APEC model with solar coronal abundances (Feldman et al. 1992), and the fit results are shown in Figure 6. For the first and fourth *NuSTAR* pointings, before and after the microflares, the spectra are well fitted by this single thermal model showing similar temperatures and emission measures (3.3 MK and  $6.3 \times 10^{46} \text{ cm}^{-3}$ , then 3.2 MK and  $7.0 \times 10^{46} \text{ cm}^{-3}$ ). Above 5 keV, there are very few counts, and this is due to a combination of the low livetime of the observations (164 and 152 s dwell time with about 2% livetime fraction resulting in effective exposures of around 3.5 s) and the high likelihood that the emission from this region peaked at this temperature before falling off very sharply at higher temperatures. These temperatures are similar to the quiescent ARs previously studied by *NuSTAR* (Hannah et al. 2016), although those regions were brighter and more numerous in the field of view, resulting in an order-of-magnitude worse livetime. The low livetime has the effect of limiting the spectral dynamic range, putting most of the detected counts at the lower energy range and no background or source counts at higher energies (Grefenstette et al. 2016; Hannah et al. 2016).

The two *NuSTAR* spectra from during the microflare, the second (impulsive phase) and third (decay phase, weaker peak), both show counts above 5 keV and produce higher temperature fits (5.1 MK and 3.5 MK). This is expected as there should be heating during the microflare, but neither fit matches the observed spectrum well, particularly during the impulsive phase. This shows that there is additional hot material during these times that a single-component thermal model cannot accurately characterize. For the spectrum during the impulsive phase, the second *NuSTAR* pointing, we tried adding additional thermal components to the fit, as shown in Figure 7. We started by adding in a second thermal component fixed with the parameters from the pre-microflare spectrum, found from the first *NuSTAR* pointing (left spectrum in Figure 6), to represent the background emission. We did this as *NuSTAR*'s pointing changed during these two times (changing the part of the detector observing the region, and hence the instrumental response) so we could not simply subtract the data from this pre-flare background time. The other thermal model component was allowed to vary and produced a slightly better fit to the higher energies and a higher temperature (5.6 MK). However, this model still misses counts at higher energies.

So, we tried another fit where the two thermal models were both allowed to vary and this is shown in the right panel of Figure 7. Here, there is a substantially better fit to the data over the whole energy range, fitting a model of 4.1 MK and 10.0 MK. The hotter model does seem to match the bump in emission between 6 and 7 keV, which at these temperatures would be due to line emission from the Fe K-shell transition (Phillips 2004). Although this model better matches the data, it produces substantial uncertainties, particularly in the emission measure. This is because it is fitting the few counts at higher energies which have a poor signal-to-noise ratio. It should be noted that for the thermal model, the temperature and emission measure are correlated and so the upper uncertainty on the

<sup>10</sup> <https://heasarc.gsfc.nasa.gov/xanadu/xspec/>

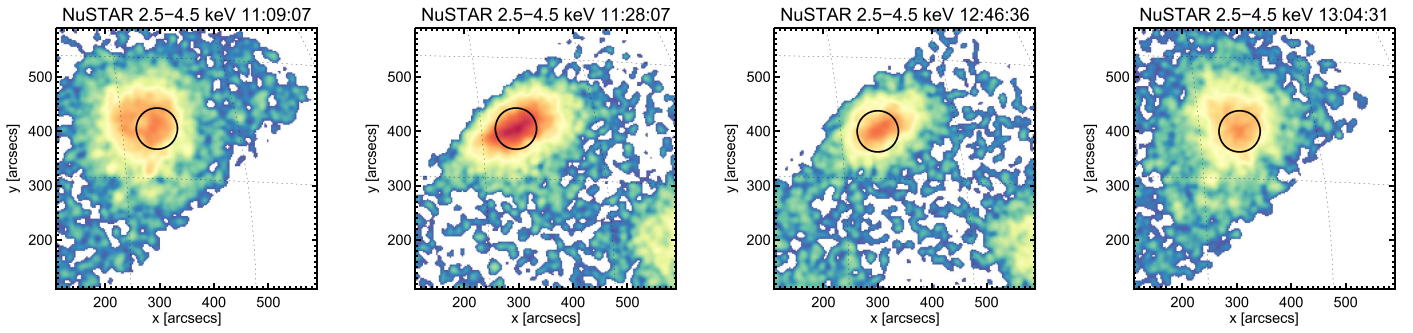


**Figure 4.** *NuSTAR* 2.5–4.5 keV maps for the four time intervals it observed AR 12333. These maps have been shifted to match the position of the *SDO*/AIA 94 Å Fe XVIII maps, shown in Figure 5. The black circles indicate the regions chosen for spectral fitting, shown in Figure 6. Note that the same color scaling is used in all these maps.

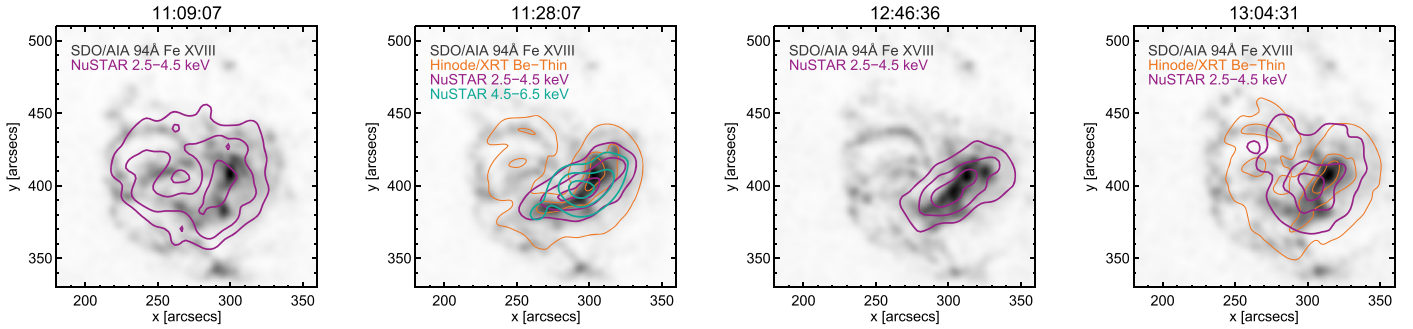


**Figure 5.** *SDO*/AIA 94 Å Fe XVIII maps overlaid with shifted contours from *Hinode*/XRT (20%, 50%, 80%; orange) and *NuSTAR* 2.5–4.5 keV and 4.5–6.5 keV emission (50%, 70%, 90%; purple, turquoise). A constant offset correction was required for *Hinode*/XRT but a different one was determined for each *NuSTAR* pointing. For the two time intervals where *NuSTAR* only observed part of the AR (middle two panels), the alignment was done using the full map and to other features on the disk.

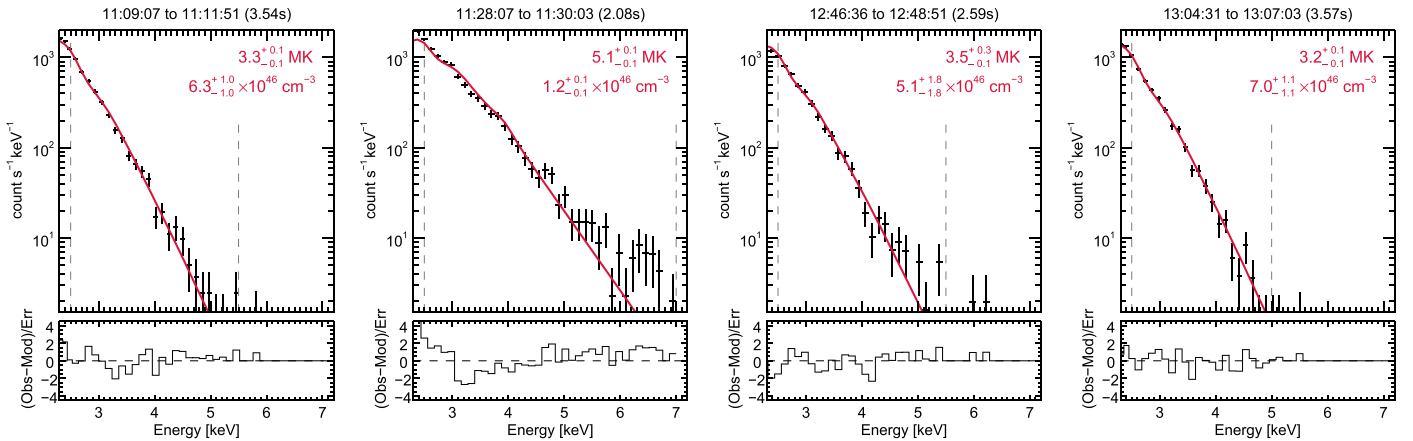


**Figure 6.** *NuSTAR* spectra for the regions shown in Figure 5, at different stages of flare evolution with time, increasing from left to right. The black data points show the combined data from FPMA and FPMB, and the red line shows the best-fit thermal model. Note that the fit to the data was performed simultaneously and is only combined for plotting. The bottom panels show the residuals, and the dashed vertical gray lines indicate the energy range over which the fit was performed (starting from the minimal usable energy of 2.5 keV up to where there are still substantial counts). The quoted uncertainties are with 90% confidence.

temperature relates to the lower uncertainty on the emission measure, and vice versa. Therefore, this uncertainty range covers a narrow diagonal region of parameter space, which we include later in Figure 11. These fits do however seem to indicate that emission from material up to 10 MK is present in this microflare and that the *NuSTAR* spectrum in this case is observing purely thermal emission. A non-thermal component could still be present, but the likely weak emission, combined with *NuSTAR*'s low livetime (limiting the spectral dynamic

range), leaves this component hidden. Upper limits to this possible non-thermal emission are calculated in Section 5.2.

From these spectral fits, we estimated the *GOES* 1–8 Å flux<sup>11</sup> to be  $5.3 \times 10^{-9} \text{ W m}^{-2}$  for the impulsive phase and  $4.0 \times 10^{-9} \text{ W m}^{-2}$  for the pre-flare time. This means that the background-subtracted *GOES* class for the impulsive phase is

<sup>11</sup> [https://hesperia.gsfc.nasa.gov/ssw/gen/idl/synoptic/goes/goes\\_flux49.pro](https://hesperia.gsfc.nasa.gov/ssw/gen/idl/synoptic/goes/goes_flux49.pro)

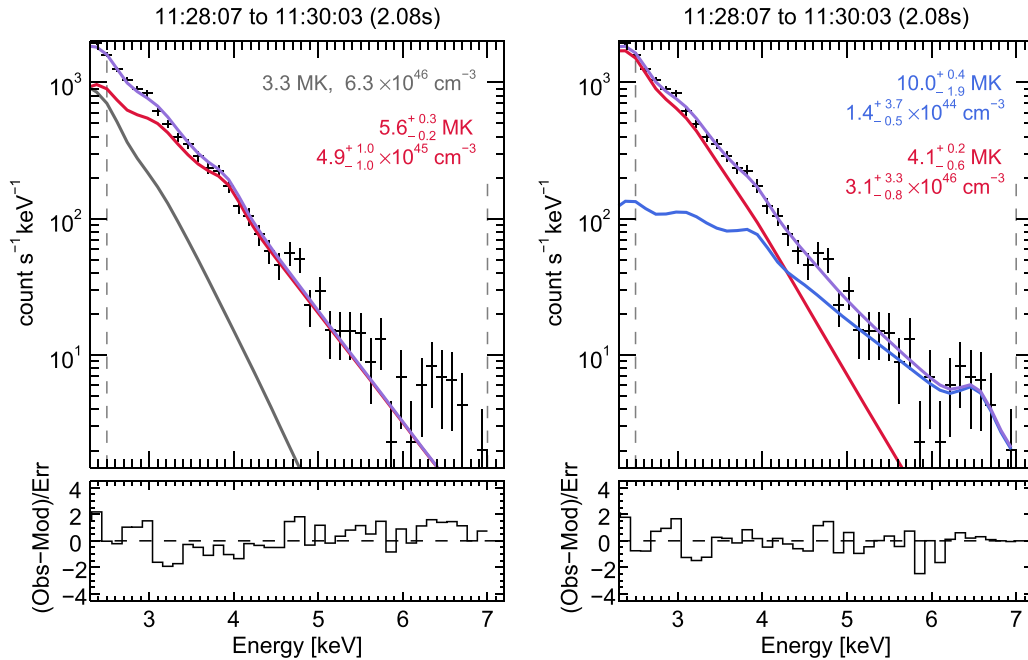


**Figure 7.** Additional model fits to the *NuSTAR* spectrum for the impulsive phase of the microflare. (Left) Model of two thermals, one fixed using the parameters from the pre-flare observation (gray line), and the second one (red) fitted. (Right) Model fitting two thermals. In both cases, the total model is shown by the purple line and the black data points show the combined data from FPMA and FPMB. Note that the fit was performed to the data simultaneously and is only combined for plotting here. The quoted uncertainties are at 90% confidence levels.

equivalent to  $\sim A0.1$  and would be slightly larger during the subsequent peak emission time.

#### 4. Multi-thermal Microflare Emission

The *NuSTAR* spectrum during the impulsive phase of the microflare clearly shows that there is a range of heated material, so to get a comprehensive view of this multi-thermal emission, we recovered the DEM by combining the observations from *NuSTAR*, *Hinode*/XRT, and *SDO*/AIA. This is the first time these instruments have been used together to obtain a DEM.

##### 4.1. Comparison of *NuSTAR*, *Hinode*/XRT, and *SDO*/AIA

To check the compatibility of the *NuSTAR*, *Hinode*/XRT, and *SDO*/AIA observations, we compared the observed fluxes from *Hinode*/XRT and *SDO*/AIA to synthetic fluxes obtained from the *NuSTAR* thermal fits. For the *NuSTAR* two-thermal fit (Figure 7, right panel), we multiplied the emission measures by the *SDO*/AIA and *Hinode*/XRT temperature response functions at the corresponding temperatures and then added the two fluxes together to get a value for each filter channel.

The *Hinode*/XRT temperature response functions were created using `xrt_flux.pro` with a CHIANTI 7.1.3 (Dere et al. 1997; Landi et al. 2013) spectrum (`xrt_flux713.pro`<sup>12</sup>) with coronal abundances (Feldman et al. 1992) and the latest filter calibrations that account for the time-dependent contamination layer present on the CCD (Narukage et al. 2014). The *SDO*/AIA temperature response functions are version 6 (v6; using CHIANTI 7.1.3) and obtained using `aia_get_response.pro` with the “chiantifix,” “eve\_norm,” and “timedepend\_date” flags. The comparison of the observed and synthetic fluxes is shown in Figure 8.

We found that the *SDO*/AIA 94 Å Fe XVIII synthetic flux is near the observed value, as expected; however, there is a consistent discrepancy for *Hinode*/XRT. The observed fluxes should match the synthetic fluxes from the *NuSTAR* spectral fits as they are sensitive to the same temperature range. Other authors have found similar discrepancies (Testa et al. 2011; Cheung et al. 2015; Schmelz et al. 2015), and there is the suggestion that the *Hinode*/XRT temperature response functions are too small by a factor of  $\sim 2$ – $3$  (see Schmelz et al. 2015). We have therefore multiplied the *Hinode*/XRT temperature response functions by a factor of two (Figure 8, top right) and find a closer match to the synthetic values derived from the *NuSTAR* spectral fits. The main effect of these larger temperature response functions is that it requires there to be weaker emission at higher temperatures to obtain the same *Hinode*/XRT flux.

##### 4.2. Differential Emission Measure

Recovering the line-of-sight DEM,  $\xi(T_j)$ , involves solving the ill-posed inverse problem,  $g_i = \mathbf{K}_{i,j}\xi(T)$ , where  $g_i$  [DN s<sup>-1</sup> px<sup>-1</sup>] is the observable and  $\mathbf{K}_{i,j}$  is the temperature response function for the  $i$ th filter channel and the  $j$ th temperature bin. Numerous algorithms have been developed for the DEM reconstruction, and we use two methods to recover the DEM: Regularized Inversion<sup>13</sup> (RI; Hannah & Kontar 2012) and the `xrt_dem_iterative2.pro` method<sup>14</sup> (XIT; Golub et al. 2004; Weber et al. 2004).

The regularized inversion (RI) approach recovers the DEM by limiting the amplification of uncertainties using linear constraints. Uncertainties on the DEM are also found on both the DEM and temperature resolution (horizontal uncertainties);

<sup>12</sup> [http://solar.physics.montana.edu/takeda/xrt\\_response/xrt\\_resp\\_ch713\\_newcal.html](http://solar.physics.montana.edu/takeda/xrt_response/xrt_resp_ch713_newcal.html)

<sup>13</sup> <https://github.com/ianan/demreg>

<sup>14</sup> [https://hesperia.gsfc.nasa.gov/ssw/hinode/xrt/idl/util/xrt\\_dem\\_iterative2.pro](https://hesperia.gsfc.nasa.gov/ssw/hinode/xrt/idl/util/xrt_dem_iterative2.pro)

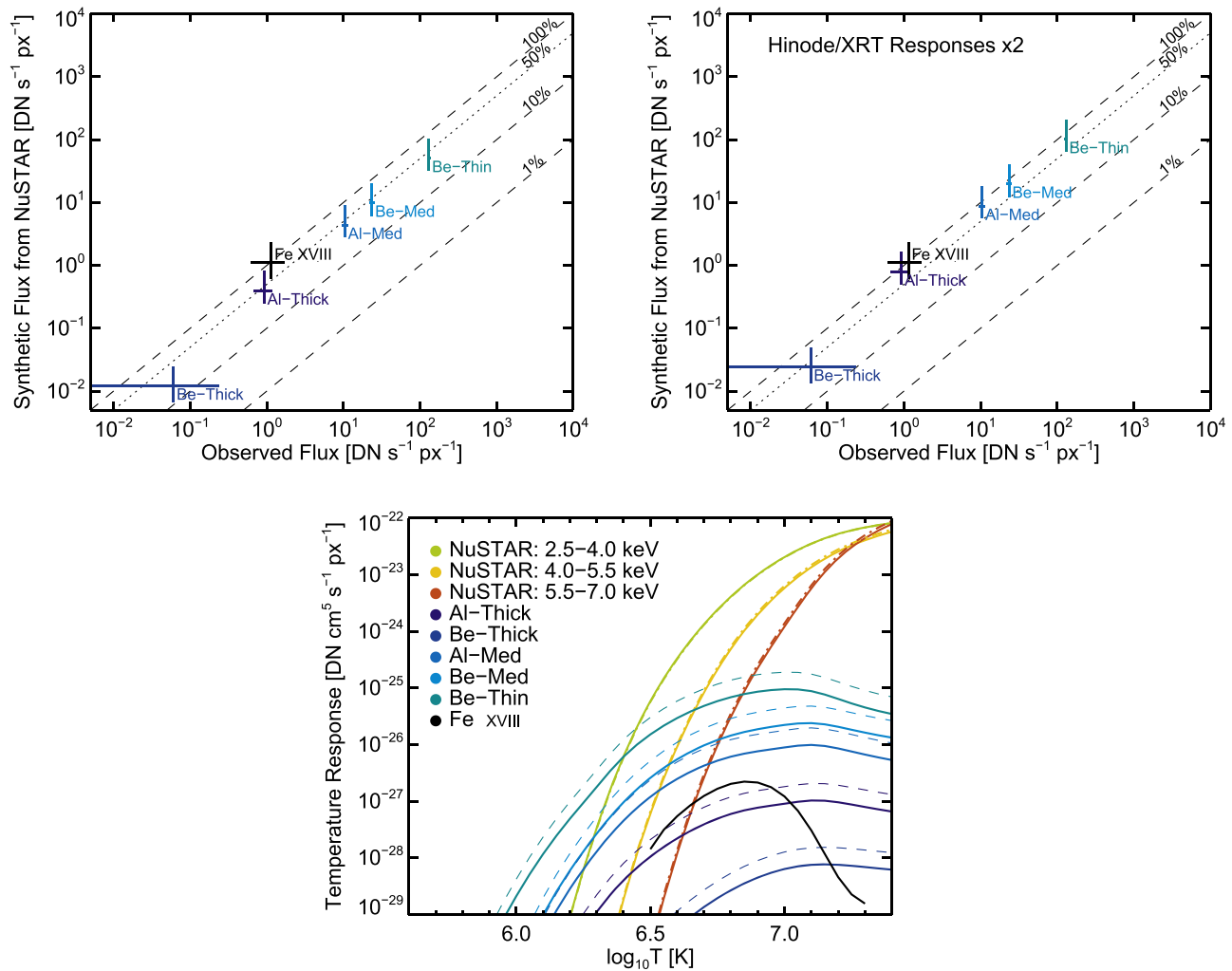


**Figure 8.** (Top) Comparison of *Hinode*/XRT and *SDO*/AIA 94 Å Fe XVIII fluxes during the microflare’s impulsive phase to the synthetic values obtained from the *NuSTAR* spectral fit. (Bottom) The temperature response functions for *NuSTAR* (FPMA, solid; FPMB, dotted-dashed), *SDO*/AIA 94 Å Fe XVIII (solid black), and *Hinode*/XRT (original, solid;  $\times 2$ , dashed) for the region shown in Figure 4 (panel 2). This has been done using the standard *Hinode*/XRT responses (top left) and then multiplying them by a factor of two (top right), which gives values closer to the observed fluxes.

see Hannah & Kontar (2012). XIT is a forward-fitting iterative least-squares approach, using a spline model. Uncertainties in the final DEM are calculated with Monte Carlo (MC) iterations with input data perturbed by an amount randomly drawn from a Gaussian distribution with the standard deviation equal to the uncertainty in the observation. The resulting spread of these MC iterations indicates the goodness of fit.

For the DEM analysis, we calculated the uncertainties on the *Hinode*/XRT and *SDO*/AIA data. The non-statistical photometric uncertainties for *Hinode*/XRT were calculated from `xrt_prep.pro` (Kobelski et al. 2014), and photon statistics were calculated from `xrt_cvfact.pro`<sup>15</sup> (Narukage et al. 2011, 2014). The uncertainties on the *SDO*/AIA data were computed with `aia_bp_estimate_error.pro` (Boerner et al. 2012), and an additional 5% systematic uncertainty was added in quadrature to both the *Hinode*/XRT and *SDO*/AIA data to account for uncertainties in the temperature response functions. The *Hinode*/XRT and *SDO*/AIA data and uncertainties have been interpolated to a common time step and averaged over the *NuSTAR* observational duration. The

uncertainty for the *NuSTAR* values in specific energy bands was determined as a combination of the photon shot noise and a systematic factor (of 5%) to account for the cross-calibration between *NuSTAR*’s two telescope modules (FPMA and FPMB). The *NuSTAR* temperature response functions for each energy range and telescope module (shown in Figure 8) were calculated using the instrumental response matrix for the regions shown in Figure 4.

The resulting DEMs obtained for the impulsive phase are shown in Figure 9 (left) with the quality of the recovered DEM solution shown as residuals between the input and recovered fluxes (right). XIT is used with the addition of 300 MC iterations where outlier XIT MC solutions have been omitted. We have used all available filters with the exception of *Hinode*/XRT Be-Thick due to large uncertainties that are the result of a lack of counts (Figure 3) and *SDO*/AIA 335 Å due to the observed long-term drop in sensitivity (see Figure 1 in Boerner et al. 2014). The standard *Hinode*/XRT responses (Figure 9, top) lead to disagreement between the two methods for DEM recovery, notably at the peak and at higher temperatures ( $\chi^2_{\text{XIT}} = 2.77$ ,  $\chi^2_{\text{RI}} = 1.01$ ). Using the *Hinode*/XRT responses multiplied by a factor of two results in the methods having much better

<sup>15</sup> Updated from CHIANTI 6.0.1 to CHIANTI 7.1.3 as part of this work.



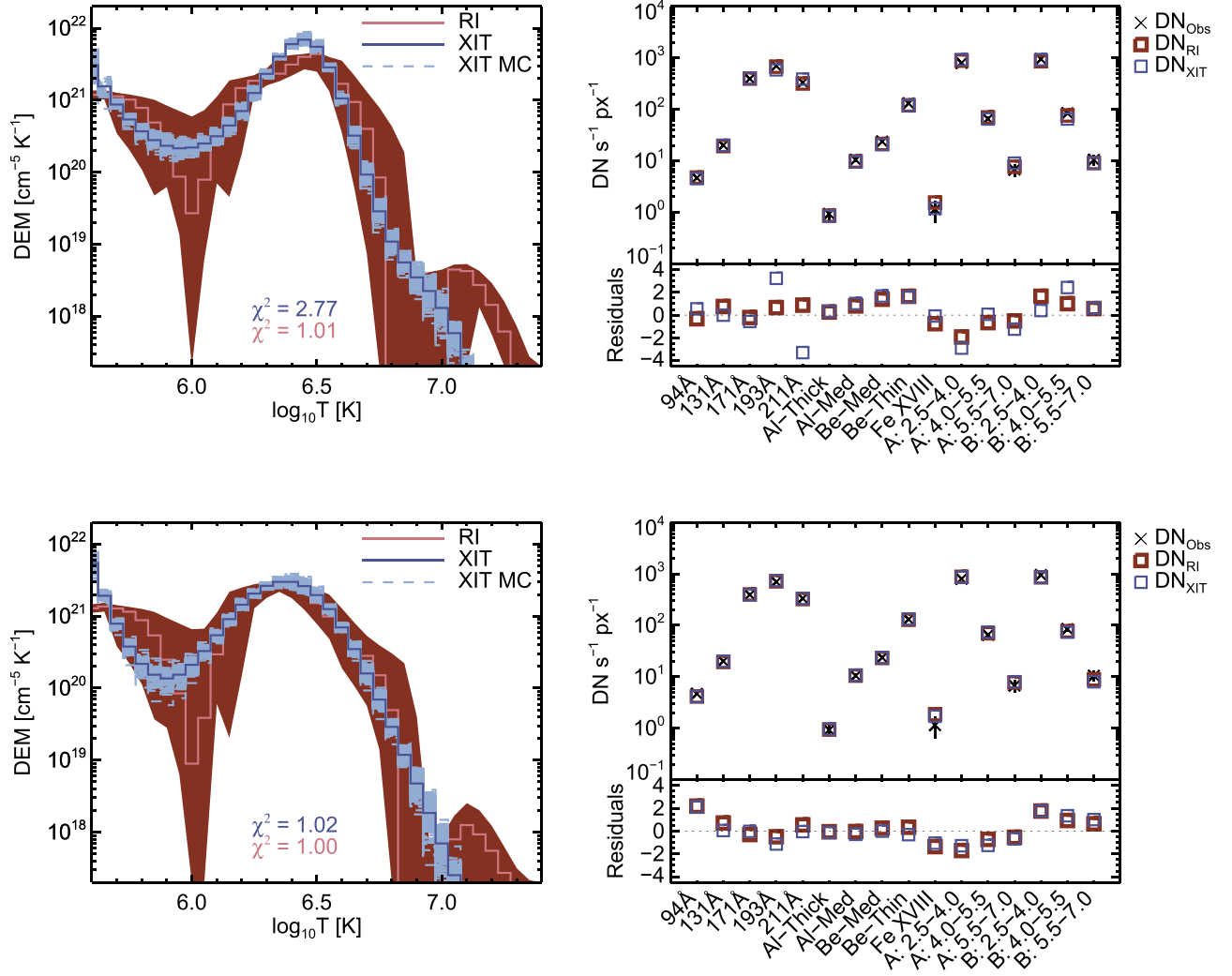


**Figure 9.** (Left) DEMs obtained during the impulsive phase of the microflare using *SDO*/AIA, *Hinode*/XRT, and *NuSTAR* data. (Right) Residuals of the DEMs in data space. The pink DEM (red error region) was obtained using the RI, and the blue (with 300 sky-blue MC iterations) from XIT. The DEMs were calculated using both the standard *Hinode*/XRT temperature responses (top) as well as those multiplied by a factor of two (bottom).

agreement ( $\chi^2_{\text{XIT}} = 1.02$ ,  $\chi^2_{\text{RI}} = 1.00$ ), and the DEM solutions result in smaller residuals, specifically in the *Hinode*/XRT filters. These final DEMs (Figure 9, bottom) show a peak at  $\sim 3$  MK and little material above 10 MK.

To understand how much of this material has been heated out of the background during the microflare, we performed DEM analysis for the pre-flare *NuSTAR* time ( $\sim 11:10$  UT). There is no *Hinode*/XRT data for this time so we determined the DEM using *NuSTAR* and *SDO*/AIA data. The DEMs for the pre-flare observations are shown in Figure 10. These DEMs for each method peak at a similar temperature ( $\sim 3$  MK) and fall off very sharply to  $\sim 5$  MK. During the microflare, there is a clear addition of material up to 10 MK (Figure 10, bottom).

We also represent the DEMs as the emission measure distributions (EMDs;  $\xi(T)dT$ ), which allows us to compare the DEM results to the *NuSTAR* spectral fits, shown in Figure 11. Here we have also overplotted the EM loci curves,  $\text{EM}_i = g_i/K_i$ , which are the upper limits of the emission based on an isothermal model, with the true solution lying below all of the EM loci curves. The *NuSTAR* thermal model fits are the isothermal (in the pre-flare phase) or two-thermal (impulsive phase) fits to the multi-thermal plasma distribution, and so

represent an approximation of the temperature distribution and emission measure. These models produce the expected higher emission measure values compared to the EMD and are consistent with the EM loci curves.

## 5. Microflare Energetics

### 5.1. Thermal Energy

For an isothermal plasma at a temperature  $T$  and emission measure EM, the thermal energy is calculated as

$$U_{Ti} = 3k_B T \sqrt{\text{EM} f V} \quad [\text{erg}], \quad (2)$$

where  $k_B$  is the Boltzmann constant,  $f$  the filling factor, and  $V$  the plasma volume (e.g., Hannah et al. 2008). Using the two-thermal fit (Figure 7, right), we calculated the thermal energy during the impulsive phase, finding  $U_{Ti} = 0.9 \times 10^{28}$  erg ( $t_i = 116$  s). Here, the equivalent loop volume,  $V_E = fV$ , was calculated as a volume of a cylinder enclosing only the flaring loop with length  $L \sim 50''$  and diameter  $d \sim 6''$ . This thermal energy includes both the microflare and background emission. We found the pre-flare energy (using fit parameters;



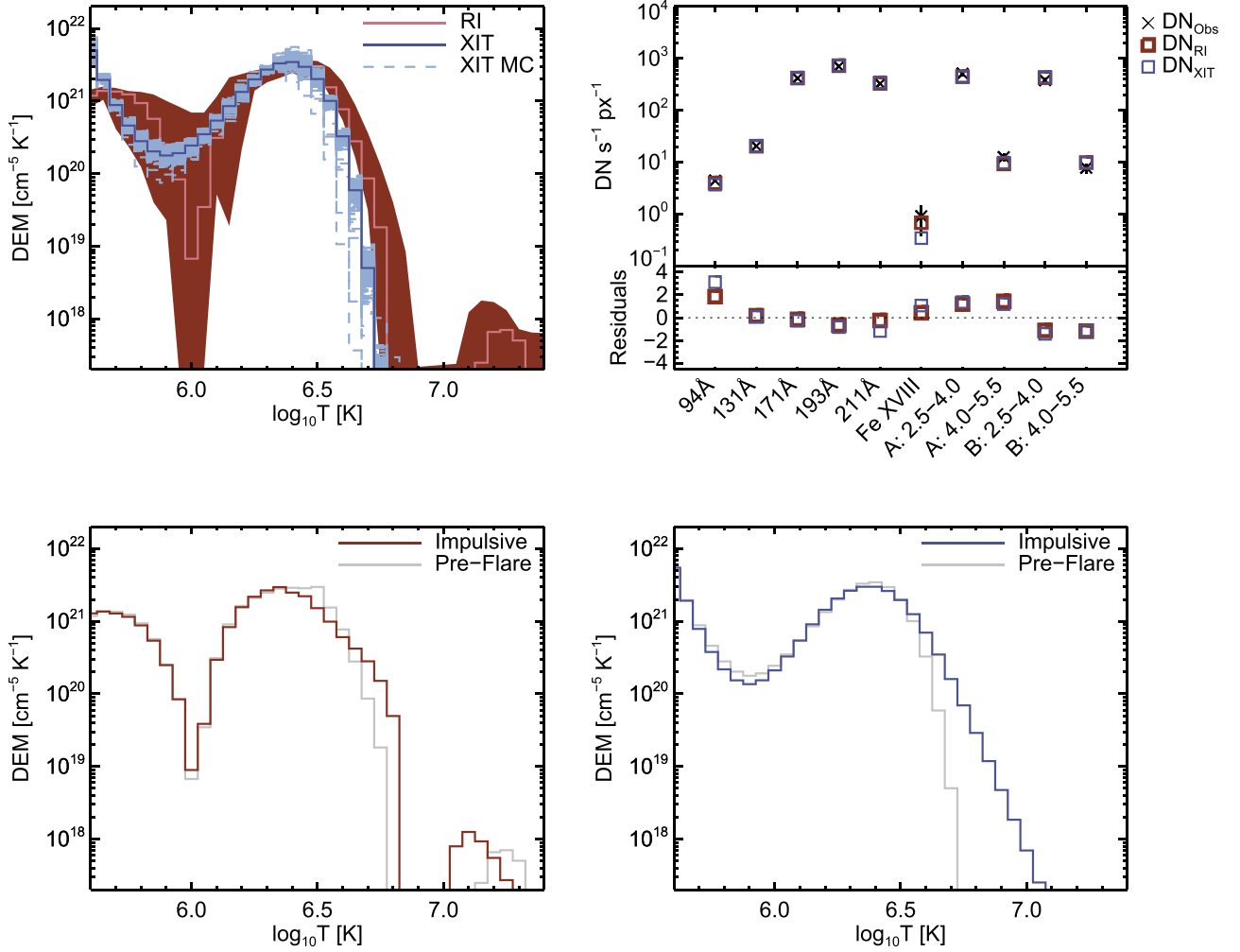


**Figure 10.** (Top left) DEM obtained from the pre-flare phase ( $\sim 11:10$  UT) using *SDO/AIA* and *NuSTAR* data. (Top right) Residuals of the DEMs in data space. (Bottom) The RI (left) and XIT (right) pre-flare DEMs shown in comparison to the impulsive-phase DEMs (Figure 9, bottom row). The pre-flare DEMs peak at similar temperatures and fall off more steeply than the impulsive-phase DEMs. The increase in the DEMs is due to the heating during the microflare.

Figure 6, left) as  $U_{T_0} = 0.9 \times 10^{28}$  erg (and  $t_0 = 164$  s). The resulting heating power during the microflare from the thermal fits to the *NuSTAR* spectra is then  $P_{T_F} = U_{T_1}/t_1 - U_{T_0}/t_0 = 2.5 \times 10^{25}$  erg s $^{-1}$ .

The thermal energy can also be estimated for a multi-thermal plasma using

$$U_T = 3k_B V_E^{1/2} \frac{\int_T T \xi_V(T) dT}{\sqrt{\int_T \xi_V(T) dT}} \quad [\text{erg}] \quad (3)$$

as described in Inglis & Christe (2014), with the filling factor,  $f = 1$ , and  $\xi_V(T) = n^2 dV/dT$  in units of cm $^{-3}$  K $^{-1}$ . For the RI and XIT DEM solutions, we find values of  $U_{T_{RI}} = 1.1 \times 10^{28}$  erg and  $U_{T_{XIT}} = 1.2 \times 10^{28}$  erg during the impulsive phase of the microflare. For the pre-flare thermal energies, we find  $U_{T_{RI0}} = 1.2 \times 10^{28}$  erg, and  $U_{T_{XIT0}} = 1.2 \times 10^{28}$  erg, and this then gives values of the heating power during the impulsive phase of the microflare as  $P_{T_{RI_F}} = 2.3 \times 10^{25}$  erg s $^{-1}$  and  $P_{T_{XIT_F}} = 3.0 \times 10^{25}$  erg s $^{-1}$ . All of these approaches give a similar value for the heating, about  $2.5 \times 10^{25}$  erg s $^{-1}$ , over the microflare's impulsive period, and a summary of these values with uncertainties are given in Table 1. It should be noted that

these values are lower limits as the estimates ignore losses during heating.

From the analysis of 25,705 *RHESSI* events (Table 1 in Hannah et al. 2008), microflare thermal energies were found to range from  $U_T = 10^{26-30}$  erg (5%–95% range; from a 16 s observation). This is equivalent to  $P_T = 6.3 \times 10^{24-28}$  erg s $^{-1}$ , and therefore the thermal power from our *NuSTAR* microflare is in the lower range of *RHESSI* observations. This is as expected as *NuSTAR* should be able to observe well beyond *RHESSI*'s sensitivity limit to small microflares.

## 5.2. *NuSTAR* Non-thermal Limits

As the *NuSTAR* spectrum in Figure 7 is well fitted by a purely thermal model, we can therefore find the upper limits of the possible non-thermal emission. This approach allows us to determine whether the accelerated electrons could power the observed heating in this microflare. We used the thick-target model of a power-law electron distribution above a low-energy cutoff  $E_c$  [keV] given by

$$F(E > E_c) \propto E^{-\delta}, \quad (4)$$

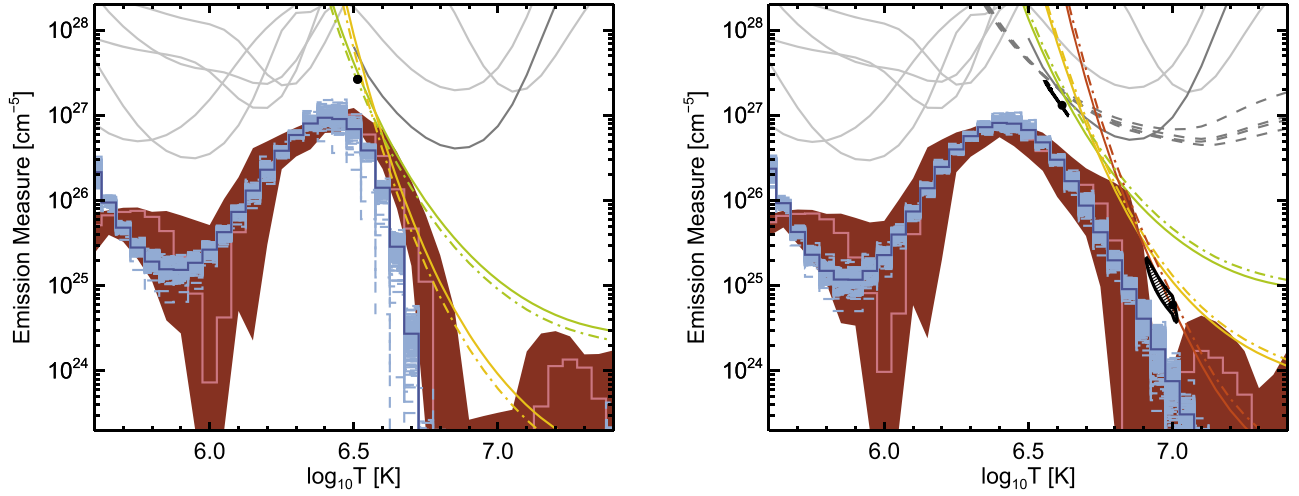


**Figure 11.** Emission measure distribution obtained from the pre-flare (left) using *SDO/AIA* and *NuSTAR* data, and the impulsive phase of the microflare (right) using *SDO/AIA*, *Hinode/XRT*, and *NuSTAR* data with the *Hinode/XRT* responses multiplied by a factor of two. The EM loci curves for *NuSTAR* are shown in the same colors as in Figure 8: the *SDO/AIA* loci are plotted in gray, with 94 Å Fe XVIII in dark gray; and *Hinode/XRT* loci are overplotted as dark gray dashed lines. The thermal fits from Figures 6 and 7 are plotted as filled circles (black) with shaded 90% confidence contours.

**Table 1**  
Summary of Thermal Energies of AR 12333

Method	$U_0^a$ [ $\times 10^{28}$ erg]	$U_T^b$ [ $\times 10^{28}$ erg]	$P_{TF}$ [ $\times 10^{25}$ erg s $^{-1}$ ]
<i>NuSTAR</i> fit	$0.9^{+0.1}_{-0.1}$	$0.9^{+0.6}_{-0.2}$	$2.5^{+5.4}_{-1.6}$
RI	$1.2^{+0.1}_{-0.1}$	$1.1^{+0.1}_{-0.1}$	$2.3^{+0.9}_{-1.0}$
XIT	$1.2^{+0.1}_{-0.1}$	$1.2^{+0.1}_{-0.1}$	$3.0^{+0.6}_{-0.7}$

**Notes.** The uncertainties on the energies and power derived from the *NuSTAR* fit are  $2.7\sigma$  (90% confidence), and those from RI/XIT are  $1\sigma$ .

<sup>a</sup> 164 s observation.

<sup>b</sup> 116 s observation.

where  $\delta$  is the power-law index, and the power in this non-thermal distribution is given by

$$P_N(>E_c) = 1.6 \times 10^{-9} \frac{\delta - 1}{\delta - 2} N_N E_c \quad [\text{erg s}^{-1}], \quad (5)$$

where  $N_N$  is the non-thermal electron flux [electrons s $^{-1}$ ].

We determined the upper limits on  $N_N$  (and  $P_N$ ) for a set of  $\delta$  ( $\delta = 5, 7, 9$ ) and  $E_c$  consistent with a null detection in the *NuSTAR* spectrum. We performed this by iteratively reducing the model electron flux  $N_N$  until there were fewer than four counts  $>7$  keV, consistent with a null detection to  $2\sigma$  (Gehrels 1986). We also ensured that the number of counts  $\leq 7$  keV are within the counting statistics of the observed counts. For each iteration, we generated the X-ray spectrum for the two-component fitted thermal model (Figure 7, right) and added to this the non-thermal X-ray spectrum for our chosen  $\delta$ ,  $E_c$ , and  $N_N$ , calculated using `f_thick2.pro`<sup>16</sup> (see Holman et al. 2011). This was then folded through the *NuSTAR* response to generate a synthetic spectrum (as discussed in Hannah et al. 2016). The upper limits are shown in Figure 12 along with the three estimates of the thermal power for the background-subtracted flare,  $P_{Tf}$  (“*NuSTAR* Fit,” black),  $P_{Tf,RI}$  (pink), and  $P_{Tf,XIT}$  (blue). For a flatter spectrum of  $\delta = 5$ , barely

any of the upper limits are consistent with the required heating power. With a steeper spectrum,  $\delta \geq 7$ , a cutoff of  $E_c \lesssim 7$  keV is consistent with the heating requirement. These steep spectra indicate that the bulk of the non-thermal emission would need to be at energies close to the low-energy cutoff to be consistent with the observed *NuSTAR* spectrum. If we instead consider some of the counts in the 6–7 keV range to be non-thermal (e.g., the excess above the thermal model in the left panel in Figure 7), then we would obtain a higher non-thermal power, about a factor of 0.5 larger. However, this would only substantially affect the steep non-thermal spectra ( $\delta \geq 7$ ) as flatter models would be inconsistent with the data below 7 keV.

We can again compare the microflare studied here to the non-thermal energetics derived from *RHESSI* microflare statistics. Hannah et al. (2008) report non-thermal parameters of  $\delta = 4$ –10 and  $E_c = 9$ –16 keV, and non-thermal power ranges from  $P_N(>E_c) = 10^{25}$ – $10^{28}$  erg s $^{-1}$ . The largest upper limits that *NuSTAR* produces for this microflare are again at the edge of *RHESSI*’s sensitivity. In a previous study of nanoflare heating, Testa et al. (2014) investigated the evolution of chromospheric and transition region plasma from *IRIS* observations using RADYN nanoflare simulations. This is one of the few non-thermal nanoflare studies, and they reported that heating occurred on timescales of  $\lesssim 30$  s, characterized by a total energy  $\lesssim 10^{25}$  erg and  $E_c \sim 10$  keV. The simulated electron beam parameters in this *IRIS* event are consistent with the *NuSTAR*-derived parameters, but in a range insufficient to power the heating in our microflare.

## 6. Discussion and Conclusions

In this paper, we have presented the first joint observations of a microflaring AR with *NuSTAR*, *Hinode/XRT*, and *SDO/AIA*. During the impulsive start, the *NuSTAR* spectrum shows emission up to 10 MK, indicating that even in this  $\sim A0.1$  microflare, substantial heating can occur. This high-temperature emission is confirmed when we recover DEMs using the *NuSTAR*, *Hinode/XRT*, and *SDO/AIA* data. These instruments crucially overlap in temperature sensitivity, with *NuSTAR* able to constrain and

<sup>16</sup> [https://hesperia.gsfc.nasa.gov/ssw/packages/xray/idl/f\\_thick2.pro](https://hesperia.gsfc.nasa.gov/ssw/packages/xray/idl/f_thick2.pro)

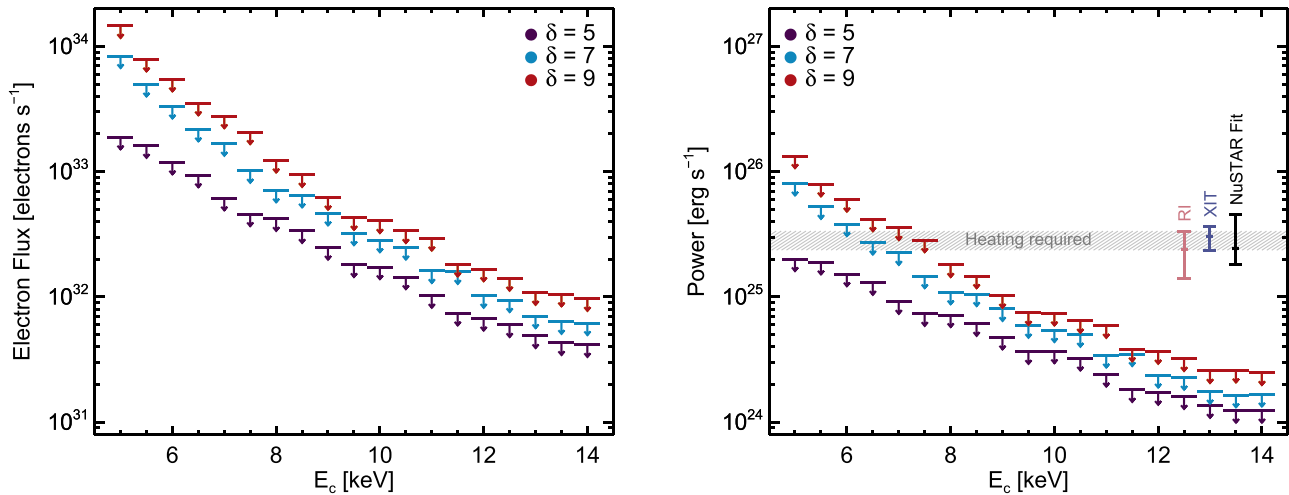


**Figure 12.** Non-thermal upper limits as a function of  $E_c$  and  $\delta$  plotted in terms of non-thermal electron flux,  $N_N$  (left), and non-thermal power,  $P_N$  (right). The three estimates for the thermal power,  $P_{TIF}$ , black;  $P_{TRIF}$ , pink; and  $P_{TXIF}$ , blue, are plotted with  $1\sigma$  uncertainties. The gray shaded region represents the required heating power, consistent with all three estimates.

characterize the high-temperature emission, which is often difficult for other instruments to do alone.

In this event, we find that the *Hinode*/XRT temperature response functions are a factor of two too small, suggesting that it would normally overestimate the contribution from high-temperature plasma in this microflare.

Overall, we find the instantaneous thermal energy during the microflare to be  $\sim 10^{28}$  erg; once the pre-flare has been subtracted this equates to a heating rate of  $\sim 2.5 \times 10^{25}$  erg s $^{-1}$  during the impulsive phase of this microflare. This is comparable to some of the smallest events observed with *RHESSI*, although *RHESSI* did not see this microflare as its indirect imaging was dominated by the brighter ARs elsewhere on the disk.

Although no non-thermal emission was detected, we can place upper limits on the possible non-thermal component. We find that we would need a steep ( $\delta \geq 7$ ) power law down to at least 7 keV to be able to power the heating in this microflare. This is still consistent with this small microflare being physically similar to large microflares and flares, but this would only be confirmed if *NuSTAR* detected non-thermal emission. To achieve this, future *NuSTAR* observations need to be made with a higher effective exposure time. For impulsive flares, this cannot be achieved with longer duration observations, only with higher livetimes. Observing the Sun when there are weaker or fewer ARs on the disk would easily achieve this livetime increase, conditions that have occurred since this observation and will continue through solar minimum.

These observations would greatly benefit from new, more sensitive, solar X-ray telescopes such as the *FOXSI* (Krucker et al. 2014) and *MaGIXS* (Kobayashi et al. 2011) sounding rockets, as well as the *MinXSS* CubeSats (Mason et al. 2016). New data combined with *NuSTAR* observations during quieter periods of solar activity should provide detection of the high-temperature and possible non-thermal emission in even smaller microflares, which should, in turn, provide a robust measure of their contribution to heating coronal loops in ARs.

This paper made use of data from the *NuSTAR* mission, a project led by the California Institute of Technology, managed by the Jet Propulsion Laboratory, and funded by the National

Aeronautics and Space Administration. We thank the *NuSTAR* Operations, Software, and Calibration teams for support with the execution and analysis of these observations. This research made use of the *NuSTAR* Data Analysis Software (NuSTAR-DAS) jointly developed by the ASI Science Data Center (ASDC, Italy), and the California Institute of Technology (USA). *Hinode* is a Japanese mission developed and launched by ISAS/JAXA, with NAOJ as domestic partner and NASA and STFC (UK) as international partners. It is operated by these agencies in cooperation with ESA and the NSC (Norway). The Atmospheric Imaging Assembly on the *Solar Dynamics Observatory* is part of NASA’s Living with a Star program. CHIANTI is a collaborative project involving George Mason University and the University of Michigan (USA), and the University of Cambridge (UK). This research made extensive use of the IDL Astronomy Library, the SolarSoft IDL distribution (SSW), and NASA’s Astrophysics Data System.

P.J.W. was supported by an EPSRC/Royal Society Fellowship Engagement Award (EP/M00371X/1) and I.G.H. was supported by a Royal Society University Fellowship. M.K. and S.K. were supported by the Swiss National Science Foundation (project number 200021-140308 and 200020-169046). A.J.M. was supported by NASA Earth and Space Science Fellowship award NNX13AM41H. This work was also supported by NASA grants NNX12AJ36G and NNX14AG07G.

The authors thank the International Space Science Institute (ISSI) for support for the team “New Diagnostics of Particle Acceleration in Solar Coronal Nanoflares from Chromospheric Observations and Modeling,” where this work benefited from productive discussions. The authors also thank P. J. A. Simões, S. H. Saar, K. K. Reeves, and J. K. Vogel for their valuable comments.

*Facilities:* *NuSTAR*, *Hinode* (XRT), *SDO* (AIA), *GOES*.

## References

- Arnaud, K. A. 1996, in ASP Conf. Ser. 101, *Astronomical Data Analysis Software and Systems V*, ed. G. H. Jacoby & J. Barnes (San Francisco, CA: ASP), 17
- Aschwanden, M. J., Tarbell, T. D., Nightingale, R. W., et al. 2000, *ApJ*, 535, 1047
- Boerner, P., Edwards, C., Lemen, J., et al. 2012, *SoPh*, 275, 41



- Boerner, P. F., Testa, P., Warren, H., Weber, M. A., & Schrijver, C. J. 2014, *SoPh*, **289**, 2377
- Cash, W. 1979, *ApJ*, **228**, 939
- Cheung, M. C. M., Boerner, P., Schrijver, C. J., et al. 2015, *ApJ*, **807**, 143
- Christe, S., Hannah, I. G., Krucker, S., McTiernan, J., & Lin, R. P. 2008, *ApJ*, **677**, 1385
- Del Zanna, G. 2013, *A&A*, **558**, A73
- Dere, K. P., Landi, E., Mason, H. E., Monsignori Fossi, B. C., & Young, P. R. 1997, *A&AS*, **125**, 149
- Feldman, U., Mandelbaum, P., Seely, J. F., Doschek, G. A., & Gursky, H. 1992, *ApJS*, **81**, 387
- Gburek, S., Sylwester, J., Kowalinski, M., et al. 2011, *SoSyR*, **45**, 189
- Gehrels, N. 1986, *ApJ*, **303**, 336
- Glencross, W. M. 1975, *ApJL*, **199**, L53
- Glesener, L., Krucker, S., Hannah, I. G., et al. 2017, *ApJ*, submitted
- Golub, L., Deluca, E., Austin, G., et al. 2007, *SoPh*, **243**, 63
- Golub, L., Deluca, E. E., Sette, A., & Weber, M. 2004, in ASP Conf. Ser. 325, *The Solar-B Mission and the Forefront of Solar Physics*, ed. T. Sakurai & T. Sekii (San Francisco, CA: ASP), 217
- Grefenstette, B. W., Glesener, L., Krucker, S., et al. 2016, *ApJ*, **826**, 20
- Hannah, I. G., Christe, S., Krucker, S., et al. 2008, *ApJ*, **677**, 704
- Hannah, I. G., Grefenstette, B. W., Smith, D. M., et al. 2016, *ApJL*, **820**, L14
- Hannah, I. G., Hudson, H. S., Battaglia, M., et al. 2011, *SSRv*, **159**, 263
- Hannah, I. G., & Kontar, E. P. 2012, *A&A*, **539**, A146
- Harrison, F. A., Craig, W. W., Christensen, F. E., et al. 2013, *ApJ*, **770**, 103
- Holman, G. D., Aschwanden, M. J., Aurass, H., et al. 2011, *SSRv*, **159**, 107
- Hudson, H. S. 1991, *SoPh*, **133**, 357
- Inglis, A. R., & Christe, S. 2014, *ApJ*, **789**, 116
- Kobayashi, K., Cirtain, J., Golub, L., et al. 2011, *Proc. SPIE*, **8147**, 1
- Kobelski, A. R., Saar, S. H., Weber, M. A., McKenzie, D. E., & Reeves, K. K. 2014, *SoPh*, **289**, 2781
- Kosugi, T., Matsuzaki, K., Sakao, T., et al. 2007, *SoPh*, **243**, 3
- Krucker, S., Benz, A. O., Bastian, T. S., & Acton, L. W. 1997, *ApJ*, **488**, 499
- Krucker, S., Christe, S., Glesener, L., et al. 2014, *ApJL*, **793**, L32
- Kuhar, M., Krucker, S., Hannah, I. G., et al. 2017, *ApJ*, **835**, 6
- Landi, E., Young, P. R., Dere, K. P., Del Zanna, G., & Mason, H. E. 2013, *ApJ*, **763**, 86
- Lemen, J. R., Title, A. M., Akin, D. J., et al. 2012, *SoPh*, **275**, 17
- Lin, R. P., Dennis, B. R., Hurford, G. J., et al. 2002, *SoPh*, **210**, 3
- Madsen, K. K., Harrison, F. A., Markwardt, C. B., et al. 2015, *ApJS*, **220**, 8
- Mason, J. P., Woods, T. N., Caspi, A., et al. 2016, *JSpRo*, **53**, 328
- Narukage, N., Sakao, T., Kano, R., et al. 2011, *SoPh*, **269**, 169
- Narukage, N., Sakao, T., Kano, R., et al. 2014, *SoPh*, **289**, 1029
- Parker, E. N. 1988, *ApJ*, **330**, 474
- Parnell, C. E., & Jupp, P. E. 2000, *ApJ*, **529**, 554
- Pesnell, W. D., Thompson, B. J., & Chamberlin, P. C. 2012, *SoPh*, **275**, 3
- Phillips, K. J. H. 2004, *ApJ*, **605**, 921
- Reale, F., Guarrasi, M., Testa, P., et al. 2011, *ApJL*, **736**, L16
- Schmelz, J. T., Asgari-Targhi, M., Christian, G. M., Dhaliwal, R. S., & Pathak, S. 2015, *ApJ*, **806**, 232
- Testa, P., De Pontieu, B., Allred, J., et al. 2014, *Sci*, **346**, 1255724
- Testa, P., & Reale, F. 2012, *ApJL*, **750**, L10
- Testa, P., Reale, F., Landi, E., DeLuca, E. E., & Kashyap, V. 2011, *ApJ*, **728**, 30
- Warren, H. P., Winebarger, A. R., & Brooks, D. H. 2012, *ApJ*, **759**, 141
- Weber, M. A., Deluca, E. E., Golub, L., & Sette, A. L. 2004, in IAU Symp. 223, *Multi-Wavelength Investigations of Solar Activity*, ed. A. V. Stepanov, E. E. Benevolenskaya, & A. G. Kosovichev (Cambridge: Cambridge Univ. Press), 321